

Transient response of partially-bonded sandwich plates subject to underwater explosions

Zhanke Liu^{a,*}, Yin L. Young^b and Michael R. Motley^a

^a*Department of Civil and Environmental Engineering, Princeton University, Princeton, NJ, USA*

^b*Department of Naval Architecture and Marine Engineering, University of Michigan, Ann Arbor, MI, USA*

Received 9 November 2008

Revised 5 June 2009

Abstract. This paper investigated the influence of interfacial bonding on the transient response of sandwich plates subject to underwater explosions. It was found that un-bonded sandwich plates receive lower impact energy, and are able to dissipate more energy through plastic deformation of the foam core, than perfectly bonded plates. Consequently, interfacial de-bonding leads to lower net energy transfer from the explosion to the target structure although it also increases the structural deformation due to stiffness reduction. Parametric studies showed that the *advantage* (diminishing of net energy transfer) is more significant than the *disadvantage* (magnification of the interface deflection). Thus, interfacial de-bonding through active/passive mechanisms may be beneficial for blast-resistant designs.

Keywords: Sandwich structures, fluid-structure interactions, underwater explosions, interface bonding, shock mitigation

1. Introduction

Sandwich plates have been suggested as an effective alternative to monolithic plates to improve the shock resistance of floating marine structures, e.g. ship hulls and decks [1,2]. A typical sandwich structure consists of two thin steel face panels connected by a low-density and compressible core. The attractiveness of sandwich plates compared to monolithic plates includes: (i) lower transmitted momentum to a sandwich plate from an explosive shock due to fluid-structure interaction, (ii) superior energy absorption and dissipation capability of the soft sandwich core, and (iii) outstanding bending/stretching strength of a sandwich plate. It has been shown that an optimally designed sandwich plate can withstand pressure impulses that are one to two times higher than an equivalent monolithic plate of the same mass and material [3]. The benefits of sandwich construction are dependent on core topologies. Most desirable topologies include periodic honeycomb and corrugated configurations [1,2].

There has been broad academic and industrial interest in the blast resistance of sandwich structures. Recent theoretical and experimental work [3–19] significantly expanded the knowledge on the dynamic response of metallic sandwich panels subject to impact and blast loads. A temporally decoupled three-stage model was proposed in [4] to quantify the shock resistance of sandwich panels. The first stage is the front face acceleration by the fluid up to cavitation inception. The second stage involves the core compression until the front and back faces reach a common velocity. The third stage brings the sandwich beam to rest by a combination of beam bending/stretching. The three-stage model was widely adopted as a framework to model the blast response of sandwich beams. It was later extended by [3,7] to consider one-dimensional sandwich structures with varying core strengths.

*Corresponding author. E-mail: zhankeliu2008@gmail.com.

While the three-stage model provides a powerful concept for uniform shocks, the sandwich plate response to underwater explosions (UNDEX) may not be temporally separable due to multi-dimensional fluid-structure interaction effects. Coupled simulations were performed in [5,7,9,14,15,18] to investigate the significance of stage coupling effects. Soft and strong core response behaviors were identified for metallic sandwich panels in [9,15,18]. For the strong core, the wet and dry faces reached a common velocity prior to the structure coming to rest; for the soft core, the dry face arrested prior to acquiring the maximum wet face velocity. The soft or strong core response depends on a number of factors, including the transverse core strength, the core thickness, the panel aspect ratio, and the magnitude of the impulse. If a slap (complete densification of a portion of the core, which can be made of a strain-rate sensitive material) can be avoided, then the soft-core design yields beneficial performance.

The recent work in [19] investigated the transient behavior of sandwich structures subject to underwater explosions, which involves significant shock-bubble-structure interaction effects. Different coupling effects, namely, the Taylor's fluid-structure interaction (FSI) effect, the bending/stretching effect, the core compression effect, and the boundary effect were quantitatively and qualitatively evaluated. Among all these effects, the Taylor's FSI effect is the most significant one. The bending/stretching effect on the interface fluid pressure oscillates with time, but it can be safely neglected for slender beams/panels. The core compression effect and boundary effect were found to increase the momentum transfer during the later stage of the transient response.

2. Objective

In the current work, numerical methodologies presented in [20,21] are adopted. The methodologies consist of a compressible Eulerian multiphase fluid solver, a nonlinear Lagrangian solid solver, and an interface coupling scheme. For completeness, the numerical models are briefly summarized below.

2.1. Fluid medium: Eulerian multiphase fluid solver

The multiphase fluid mixture is assumed to be inviscid and nonlinearly compressible, which is governed by the system of compressible Euler equations. The multiphase Euler model is used instead of typical acoustic fluid model due to the need to capture the effects of nonlinear compressibility and complex shock-bubble-fluid-structure interactions. The 2D compressible Euler equations can be written in conservative vectorial form as follows:

$$\begin{aligned} \mathbf{o} &= \frac{\partial \mathbf{U}}{\partial t} + \frac{\partial \mathbf{F}}{\partial x} + \frac{\partial \mathbf{G}}{\partial y} \\ \mathbf{U} &= [\rho, \rho u, \rho v, E]^T \\ \mathbf{F} &= [\rho u, p + \rho u^2, \rho uv, u(E + p)]^T \\ \mathbf{G} &= [\rho v, \rho uv, p + \rho v^2, v(E + p)]^T \end{aligned} \quad (1)$$

where p , ρ , u , and v are the flow pressure, density, velocity in the x direction, and velocity in the y direction, respectively. The mixture density is calculated as $\rho = \alpha \rho_g + (1 - \alpha) \rho_l$, where ρ_g and ρ_l are the densities of the liquid and gas phases, respectively, and α is the void fraction. Notice that $\alpha = 0$ corresponds to a pure liquid and $\alpha = 1$ corresponds to a pure gas. The total energy is defined as $E = \rho e + \rho(u^2 + v^2)/2$, where e is the specific internal energy (per unit mass).

Equations of state (EOS) used in the current work include the ideal gas law (Eq. (2)), the barotropic Tait's EOS (Eq. (3)), and the isentropic one-fluid cavitation model (Eq. (4)) for the gas, liquid, and cavitation mixture, respectively:

$$p = (\gamma_g - 1) \rho e \quad (2)$$

$$p = B(\rho/\rho_0)^{\gamma_l} - B + A \quad (3)$$

$$\rho = \frac{K \rho_g^{cav} + \rho_l^{cav}}{\left(\frac{\bar{p}}{p_{cav}}\right)^{-1/\gamma_l} + K \left(\frac{\bar{p}}{p_{cav}}\right)^{-1/\gamma_g}} \quad (4)$$

where $\gamma_g = 1.4$ is the ratio of specific heat of gas and $\rho_0 = 1000kg/m^3$ is the reference liquid density. The model parameters A , B , and γ_l are set equal to $1.01 \times 10^5 Pa$, $3.31 \times 10^8 Pa$, and 7.0, respectively. In Eq. (4), $K = \alpha_0/(1 - \alpha_0)$ is dynamically adjusted using the method presented in [22], where α_0 is the void fraction of the cavitation mixture at the cavitation pressure p_{cav} ; ρ_g^{cav} and ρ_l^{cav} are respectively the associated gas and liquid densities, respectively, at the cavitation pressure p_{cav} ; $\bar{p} = p + \bar{B}$, $\bar{p}_{cav} = p_{cav} + \bar{B}$, and $\bar{B} = B - A$.

2.2. Sandwich structure: Lagrangian nonlinear solid solver

The deformable solid structure is governed by the Cauchy's stress equations of motion supplemented with proper constitutive and kinematic relations. It is a general hyperbolic initial boundary value problem, which takes the following strong form:

$$\begin{aligned}
 \rho_s \ddot{\boldsymbol{\delta}} &= \nabla \cdot \boldsymbol{\sigma} & \text{on } \Omega \times]0, T[\\
 \boldsymbol{\delta} &= \mathbf{g} & \text{on } \Gamma_g \times]0, T[\\
 \boldsymbol{\sigma} &= \mathbf{h} & \text{on } \Gamma_h \times]0, T[\\
 \boldsymbol{\delta}(\mathbf{x}, 0) &= \boldsymbol{\delta}_0(\mathbf{x}) & \mathbf{x} \in \Omega \\
 \dot{\boldsymbol{\delta}}(\mathbf{x}, 0) &= \dot{\boldsymbol{\delta}}_0(\mathbf{x}) & \mathbf{x} \in \Omega
 \end{aligned} \tag{5}$$

where $\boldsymbol{\delta}$, $\dot{\boldsymbol{\delta}}$, and $\ddot{\boldsymbol{\delta}}$ are the Lagrangian solid nodal displacement, velocity, and acceleration vectors, respectively; ρ_s and $\boldsymbol{\sigma}$ are the solid density and Cauchy stress tensor; Γ_g and Γ_h are the Dirichlet and Neumann boundaries, respectively; \mathbf{g} and \mathbf{h} are the prescribed displacement and traction boundary conditions, respectively; \mathbf{x} and Ω are the solid spatial coordinates and computational domain, respectively; $\boldsymbol{\delta}_0$ and $\dot{\boldsymbol{\delta}}_0$ are the initial solid displacement and velocity vectors, respectively. Notice that the body force is assumed to be negligible compared to the explosion forced in the current work.

For elastic-plastic rate-independent material behavior, the stress-strain relation can be expressed as $\boldsymbol{\sigma} = \mathbf{C}\boldsymbol{\epsilon}^{el} = \mathbf{C}(\boldsymbol{\epsilon} - \boldsymbol{\epsilon}^{pl})$, where \mathbf{C} is elastic stiffness matrix; $\boldsymbol{\epsilon}$, $\boldsymbol{\epsilon}^{el}$, and $\boldsymbol{\epsilon}^{pl}$ are the total logarithmic strain tensor, elastic logarithmic strain tensor, and plastic logarithmic strain tensor, respectively. Notice that the classical additive property of strain has been assumed, i.e., $\boldsymbol{\epsilon} = \boldsymbol{\epsilon}^{el} + \boldsymbol{\epsilon}^{pl}$. For rate dependent material behavior, the total logarithmic strain rate $\dot{\boldsymbol{\epsilon}}$ is the sum of the elastic logarithmic strain rate $\dot{\boldsymbol{\epsilon}}^{el}$ and the plastic logarithmic strain rate $\dot{\boldsymbol{\epsilon}}^{pl}$, i.e., $\dot{\boldsymbol{\epsilon}} = \dot{\boldsymbol{\epsilon}}^{el} + \dot{\boldsymbol{\epsilon}}^{pl}$. The over-stress visco-plastic model presented in [7,10] is adopted in the current work. The elastic and plastic strain rates are respectively calculated as $\dot{\boldsymbol{\epsilon}}^{el} = \dot{\boldsymbol{\sigma}}/\mathbf{C}$ and $\dot{\boldsymbol{\epsilon}}^{pl} = \max[0, (\boldsymbol{\sigma} - \boldsymbol{\sigma}_c)/\eta_v]$, where $\boldsymbol{\sigma}_c$ is the yield stress and η_v is the viscosity coefficient.

The general finite element discrete equations in matrix form for Eq. (5) can be obtained by virtue of proper constitutive and kinematic relations:

$$\begin{aligned}
 \mathbf{M}\ddot{\boldsymbol{\delta}} + \mathbf{K}\boldsymbol{\delta} &= \mathbf{F} \quad \text{for } t \in [0, T] \\
 \boldsymbol{\delta}(0) &= \boldsymbol{\delta}_0 \quad \text{at } t = 0 \\
 \dot{\boldsymbol{\delta}}(0) &= \dot{\boldsymbol{\delta}}_0 \quad \text{at } t = 0
 \end{aligned} \tag{6}$$

where $\mathbf{M} = \int_{\Omega} \mathbf{N}^T \rho_s \mathbf{N} dV$ and $\mathbf{K} = \int_{\Omega} \mathbf{B}^T \mathbf{C} \mathbf{B} dV$ are the solid mass and stiffness matrices, respectively, and $\mathbf{F} = \int_{\Gamma_h} \mathbf{N} \mathbf{h} d\Gamma$ is the external force vector. In these matrix representations, \mathbf{N} is the displacement interpolation matrix, \mathbf{B} is the strain-displacement matrix, and \mathbf{h} is the surface traction vector. The effect of structural damping is neglected in Eq. (6). It should be noted that both geometric and material nonlinearities, as well as fluid-structure interaction effects, are considered in the current model. Hence, both \mathbf{K} and \mathbf{F} are functions of the structural response.

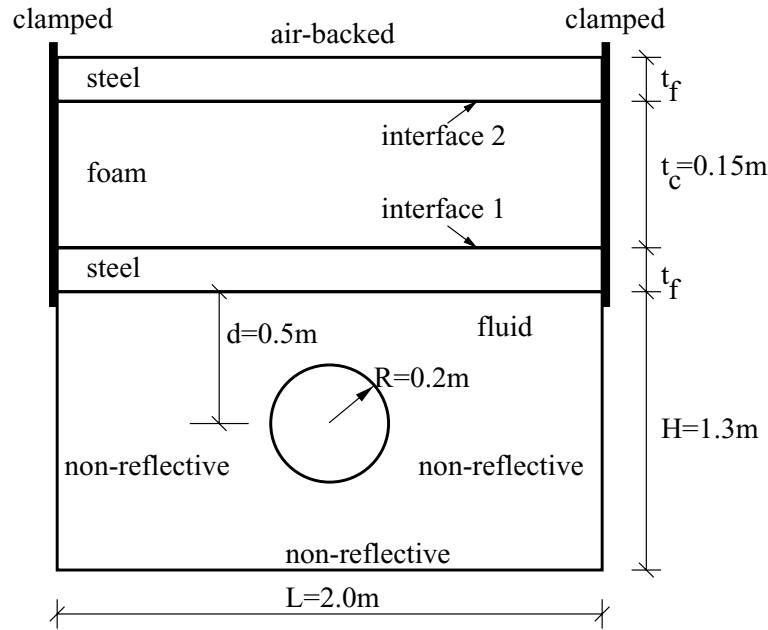


Fig. 1. Schematic drawing for the simulated model configuration.

2.3. GAS-fluid and fluid-solid interface treatments

To treat the dynamic gas-water and cavity-water interfaces using the multiphase Euler solver on a fixed Cartesian mesh, a modified ghost fluid method (MGFM) [23] is adopted in the current work. To capture the moving interfaces, the level set technique [24] is utilized. The MGFM treats the moving interfaces as ‘invisible’ internal boundaries embedded in a fixed Eulerian grid, and employs a double-shock approximate Riemann solver to determine the interface fluid status. The predicted interface status is then used to define the fluid status in a narrow band of ghost fluid cells near the interface. Thus, typical higher-order numerical schemes (such as total variation diminishing (TVD) or essentially non-oscillatory (ENO) schemes) can be conveniently applied.

For the fluid-solid interface, the interface motion is determined by the Lagrangian FEM solver. The pressure and normal velocity equilibrium conditions are imposed at the fluid-solid interface. The fluid characteristic equation and the solid equation of motion are solved together to achieve strong coupling between the Eulerian fluid and Lagrangian solid solvers. Moving Lagrangian FEM elements are only distributed over the solid domain. Fixed Eulerian fluid cells are distributed over both the fluid and solid domains. The Eulerian fluid cells are divided into two groups, namely the real fluid cells and the ghost fluid cells. Only a narrow band of ghost fluid cells on the solid side of the fluid-solid interface are solved for. The number of ghost fluid cells required depends on the order of the numerical scheme used in the fluid calculation. The ghost fluid cells outside the narrow band are not solved for, but they exist to allow the moving fluid-solid interface to be treated as an internal boundary in the fixed-grid Eulerian fluid solver. The current method is robust and efficient since it can treat highly deforming fluid-fluid and fluid-solid interfaces using a fixed fluid mesh. Details of the methods can be found in [20,21].

3. Results and discussions

3.1. Model configurations

A schematic drawing of the model configuration is shown in Fig. 1, where an underwater explosion is occurring below an air-backed three-layer sandwich plate with clamped ends. The sandwich plate is composed of two steel face layers and an in-between soft foam core. The fluid domain is in contact with the bottom steel face layer. The

plate length and the thicknesses of the foam core were taken to be $L = 2.0$ m and $t_c = 0.15$ m, respectively. Notice that different thickness of steel face layers was simulated, including $t_f = 0.025$ m, $t_f = 0.030$ m, and $t_f = 0.035$ m, to study the influence of different face-to-core thickness ratios. Details can be found in the results section. The density, Young's modulus, Poisson's ratio, and yield strength of the steel face panels were taken to be $\rho_f = 8000$ kg/m³, $E_f = 210$ GPa, $\nu_f = 0.27$, and $\sigma_f = 900$ MPa, respectively. No strain hardening was considered for the steel panels. The core structure was assumed to be made of Alporas aluminum foam [10], which has a density of $\rho_c = 236$ kg/m³, Young's modulus of $E_c = 10$ GPa, Poisson's ratio of $\nu_c = 0.0$, plateau yield strength of $\sigma_c = 1.5$ MPa, and densification strain of $\epsilon_c = 0.8$. An over-stress visco-plastic model was used to account for the rate dependence of the core material [10,20]. The fluid domain is located below the bottom steel face plate. It has horizontal and vertical lengths of 2.0 m and 1.5 m, respectively. Notice that the real and ghost fluid domains have initial heights of 1.3 m and 0.2 m, respectively. Only the real fluid is shown in in Fig. 1. The ghost fluid with a thickness of 0.2 m (not shown) is located just above the initial fluid-steel interface. The initial high-pressure gas bubble was assumed to be located at 0.5 m below the initial lower (incident) fluid-solid interface, with an initial pressure of 500 bar and an initial radius of 0.2 m.

3.2. Simulated cases

As indicated in Fig. 1, there are two foam-steel interfaces, namely, interface 1 and interface 2. To study the influence of interface bonding, four configurations are simulated and compared:

- Case I: perfect-bonding at interface 1 and perfect-bonding at interface 2;
- Case II: no-bonding at interface 1 and no-bonding at interface 2;
- Case III: perfect-bonding at interface 1 and no-bonding at interface 2;
- Case IV: no-bonding at interface 1 and perfect-bonding at interface 2.

Comparison between Cases I and II will illustrate the significance of interface bonding on the system behavior. Comparison between Cases III and IV will reveal the relative importance of the two bonding interfaces, 1 and 2, on the energy dissipation.

To study the effectiveness of partial interface bonding, two schemes as illustrated in Fig. 2 are simulated. The total length of un-bonded interfaces is L_{nb} , which is a fraction of the total panel length L , for both schemes *A* and *B*. The only difference is the distribution of the un-bonded areas. For scheme *A*, two intervals of un-bonded interface with equal length of $0.5L_{nb}$ are divided by an interval of bonded interface; for scheme *B*, a single interval of un-bonded interface with a length of L_{nb} is located at the central portion of the sandwich plate. Different response behaviors corresponding to these two schemes are compared and discussed in the results section.

3.3. Convergence studies

A numerical convergence study is first carried out to determine the spatial and temporal step sizes for accurate and stable simulations. Case I is chosen for the convergence study. Three meshes are examined:

- mesh I: fluid: 240×180 ; solid: 60×21 ;
- mesh II: fluid: 360×270 ; solid: 90×35 ;
- mesh III: fluid: 480×360 ; solid: 120×42 .

The time steps are taken to be $0.4 \mu s$, $0.3 \mu s$, and $0.2 \mu s$, respectively for meshes I, II, and III, to maintain the same *CFL* number. As shown in Fig. 3, the results are insensitive to the time step sizes as long as stability is guaranteed. Notice that the eight-node brick elements with reduced integration (C3D8R) available in ABAQUS/Explicit [25] are used. The fluid pressure at the mid-span of the fluid-solid interface is recorded for comparison between different grid densities. As shown in Fig. 3, the mid-span fluid pressure converged at mesh III. Hence, the fluid and solid meshes are taken to be 480×360 and 120×42 , respectively, from here on. The time step size is taken to be $0.2 \mu s$.

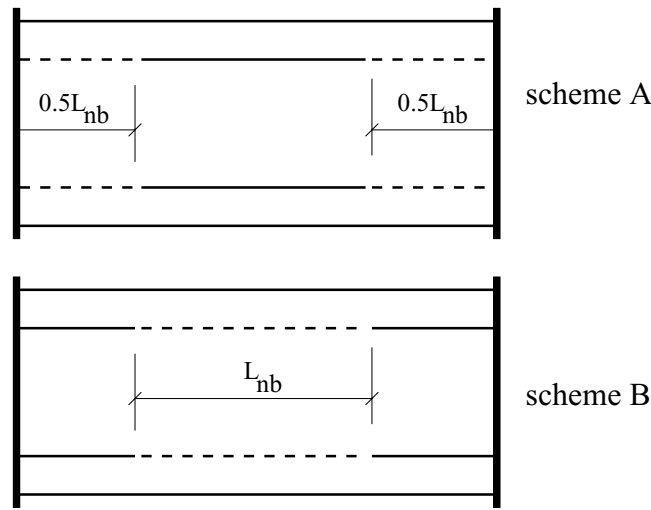


Fig. 2. Schematic drawing for the partially-bonded interfaces (Notice that $0 \leq L_{nb} \leq L$ varies as a fraction of the total panel length L , for both schemes *A* and *B*. Results of parametric studies are shown in Fig. 21).

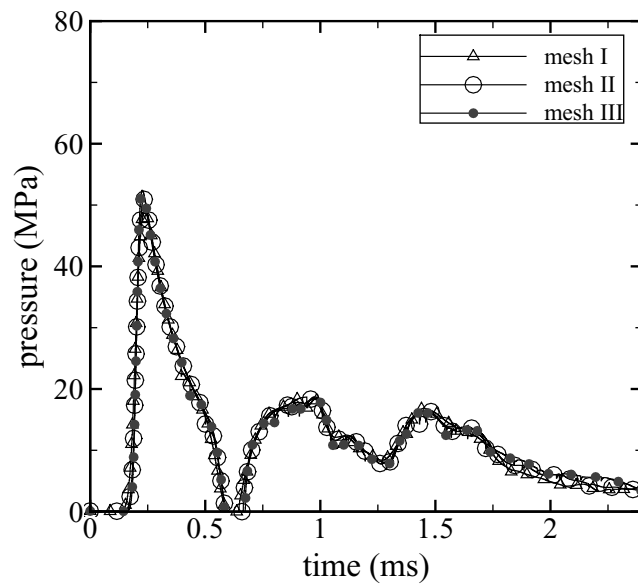


Fig. 3. Grid convergence study of the wet face pressure at the mid-span.

3.4. Structural and fluid dynamics: Perfect-bonding vs no-bonding

The comparisons of wet (incident/front) face pressure histories between the perfect- and no-bonding plates are shown in Figs 4 and 5, respectively, for the mid-span and quarter-span. It can be seen that for the initial stage ($t < 1.0$ ms), the pressure difference is small between the perfect- and no-bonding plates. In the later plate bending/stretching and core compression stages, the no-bonding sandwich plate is subject to slightly lower wet face pressure than the perfect-bonding plate in general. This reduction in wet face pressure is more consistent at the quarter-span (Fig. 5) than at the mid-span (Fig. 4). This is because the slip due to loss of interfacial bonding is zero at the center and at the ends, while its magnitude accumulates and becomes more significant near the quarter-span. To visualize the spatial pressure distribution, Fig. 6 presents the comparison of the fluid-solid interface pressure profiles at $t = 0.4$ ms and $t = 1.5$ ms. Again, for the initial stage ($t = 0.4$ ms), no visible difference exists between the

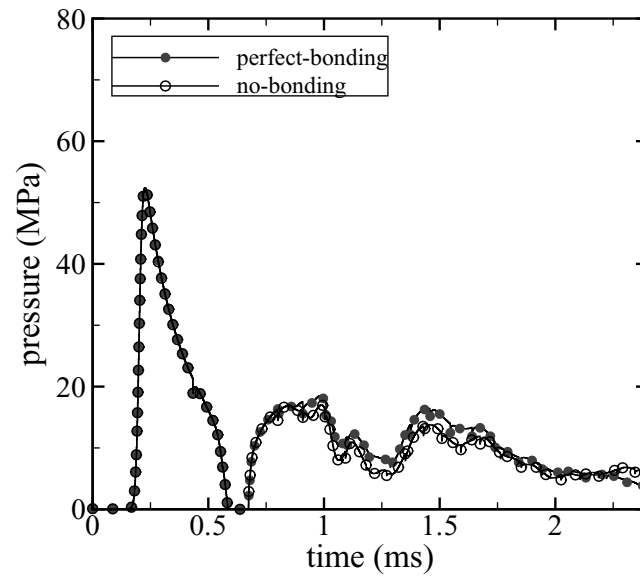


Fig. 4. Comparison of the front face pressure history at mid-span between the perfect- and no-bonding sandwich plates with clamped ends.

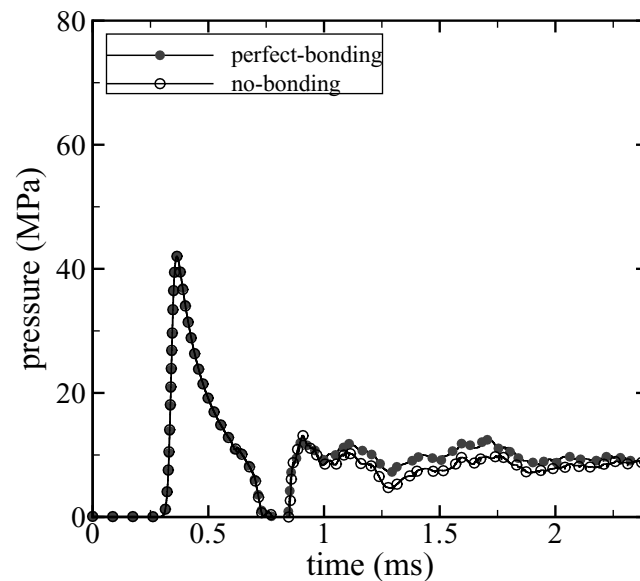


Fig. 5. Comparison of the front face pressure history at quarter-span between the perfect- and no-bonding sandwich plates with clamped ends.

perfect- and no-bonding plates. At $t = 1.5$ ms, the wet face pressure for the no-bonding plate is consistently lower than that for the perfect-bonding plate.

Though the perfect-bonding plate is subject to slightly higher pressures, its front (wet) face velocity is lower than the no-bonding plate as shown in Fig. 7. This is due to the higher rigidity of the perfect-bonding plate. The faster and more effective momentum transfer from the front face via the foam core to the back (dry) face caused the back face velocity of the perfect-bonding plate to be higher than the no-bonding plate. By the end of the simulation, the back and front faces reach a common velocity for the perfect-bonding plate due to strong interaction arising from perfect bonding. On the contrary, for the no-bonding plate, a common velocity has not yet been reached between the two faces due to weaker interactions. The displacement histories are plotted in Fig. 8, which exhibit similar

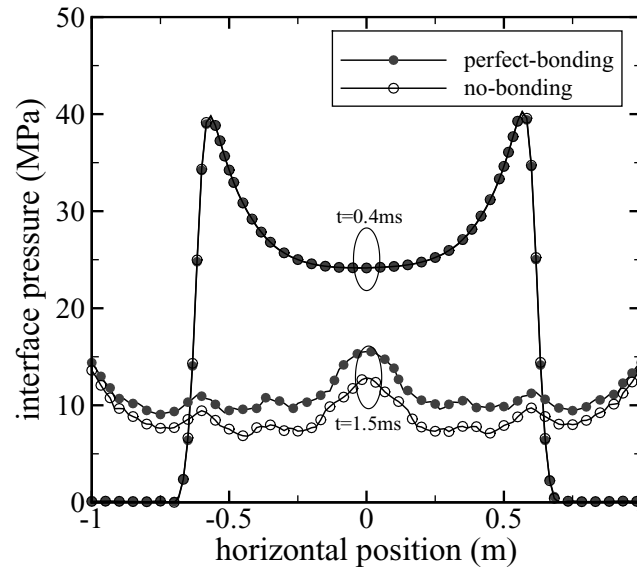


Fig. 6. Comparison of the fluid-solid interface pressure profiles between the perfect- and no-bonding sandwich plates with clamped ends.

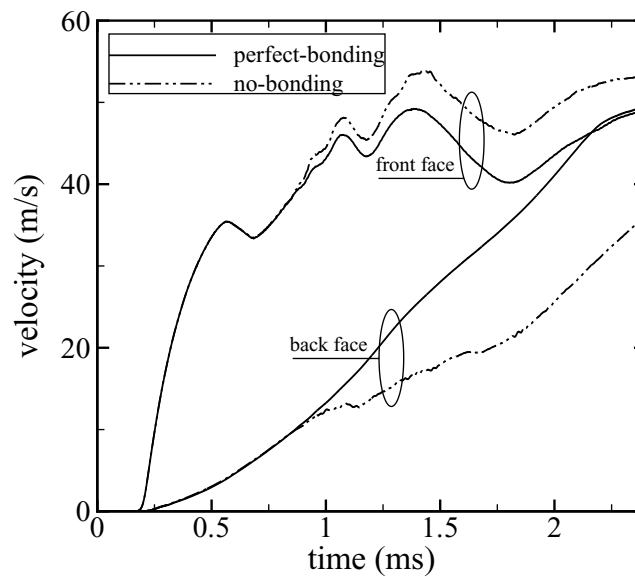


Fig. 7. Comparison of the mid-span velocity history between the perfect- and no-bonding sandwich plates with clamped ends.

behaviors due to the above mentioned reasons.

The different deformation characteristics lead to different nominal core compressive strain histories as shown in Fig. 9. The foam core of the no-bonding plate is compressed much more at the mid-span than the perfect-bonding plate due to larger deformation of the front face and smaller deformation of the rear face. The core compression phase ends approximately at $t = 1.5$ ms for the perfect bonding plate when the front and back steel faces reach a common velocity. On the contrary, the nominal core compression strain continues to increase for the no-bonding plate. The loss of interface bonding gives rise to different energy transfer histories as shown in Fig. 10. It can be seen that less work is being done to the no-bonding plate by the underwater explosion due to lower wet face pressure. In addition, more energy is dissipated for the no-bonding plate via plastic deformation of the foam core

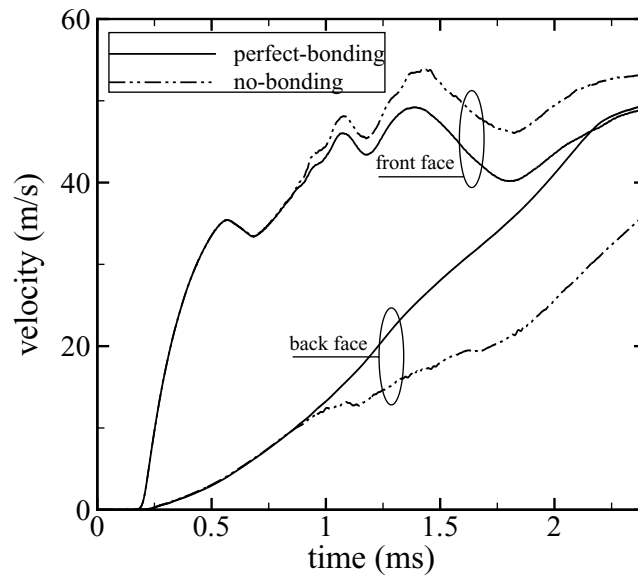


Fig. 8. Comparison of the mid-span displacement history between the perfect- and no-bonding sandwich plates with clamped ends.

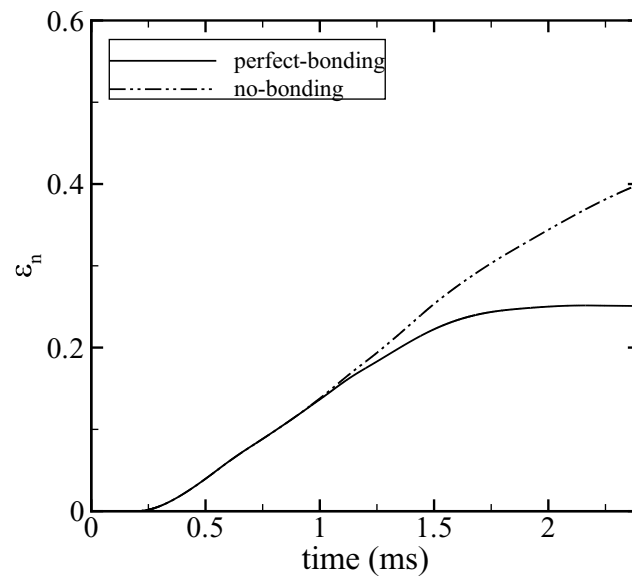


Fig. 9. Comparison of the mid-span nominal compressive strain ϵ_n history of the foam core between the perfect- and no-bonding sandwich plates with clamped ends.

due to higher degree of core compression. This leads to much lower net energy gaining by the no-bonding plate than by the perfect-bonding plate from the *UNDEX*.

The fluid fields (pressure contours, velocity vectors, bubble configurations, and interface positions) are presented from Figs 11 to 14 for different time instances. Due to symmetry, only half of the computational domain is plotted. On the left side is the perfect-bonding plate and on the right side is the no-bonding plate. The contour levels are for the fluid pressure. The vectors correspond to the fluid velocity. The dashed circle represents the initial bubble while the solid circle represents the expanded bubble. A comparison shows that the fluid response remains almost the same between the perfect- and no-bonding plates for the early stage ($t = 0.4$ ms and $t = 0.7$ ms). For both the

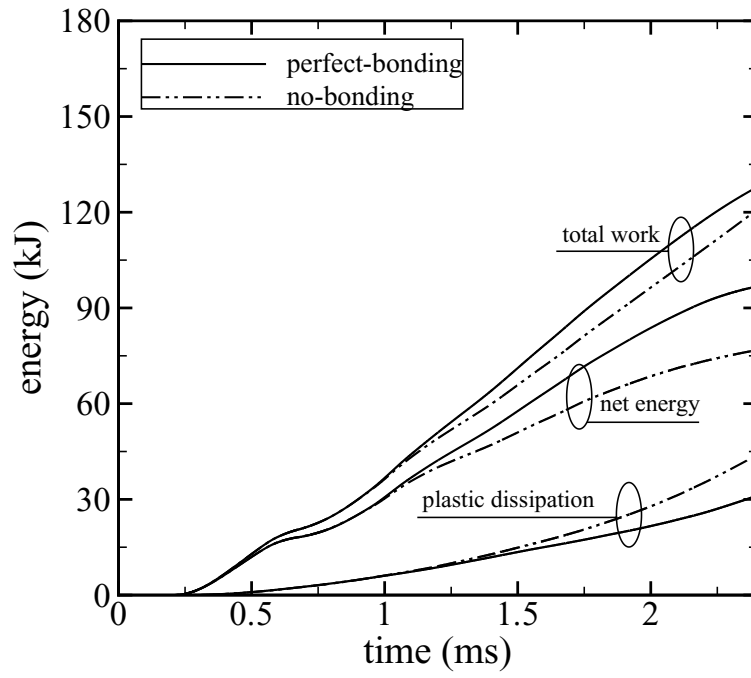


Fig. 10. Comparison of energy transfer time histories between the perfect- and no-bonding sandwich plates with clamped ends.

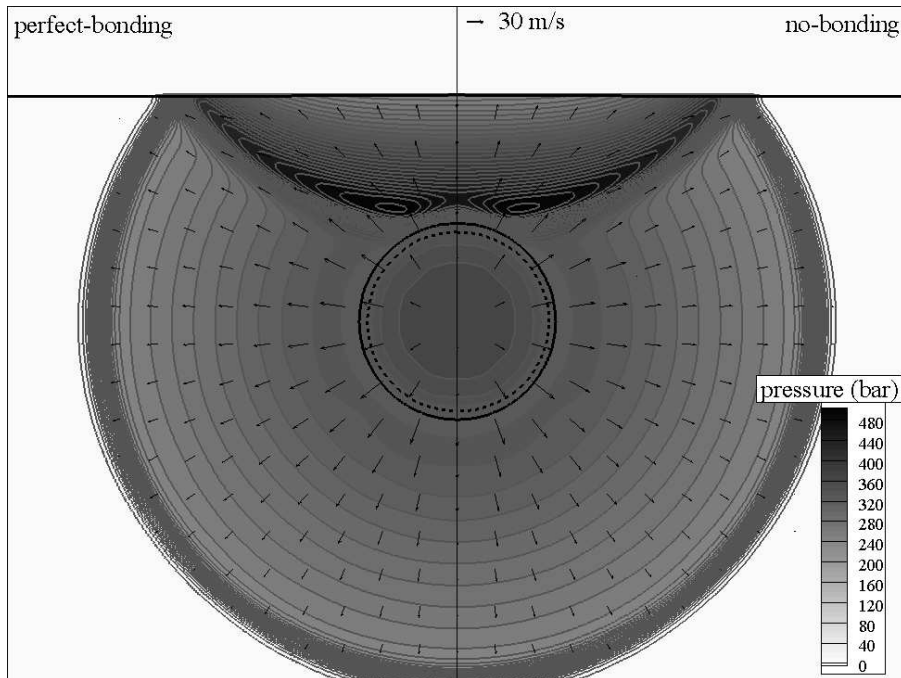


Fig. 11. Comparison of the fluid fields at $t = 0.4$ ms between the perfect- and no-bonding sandwich plates with clamped ends.

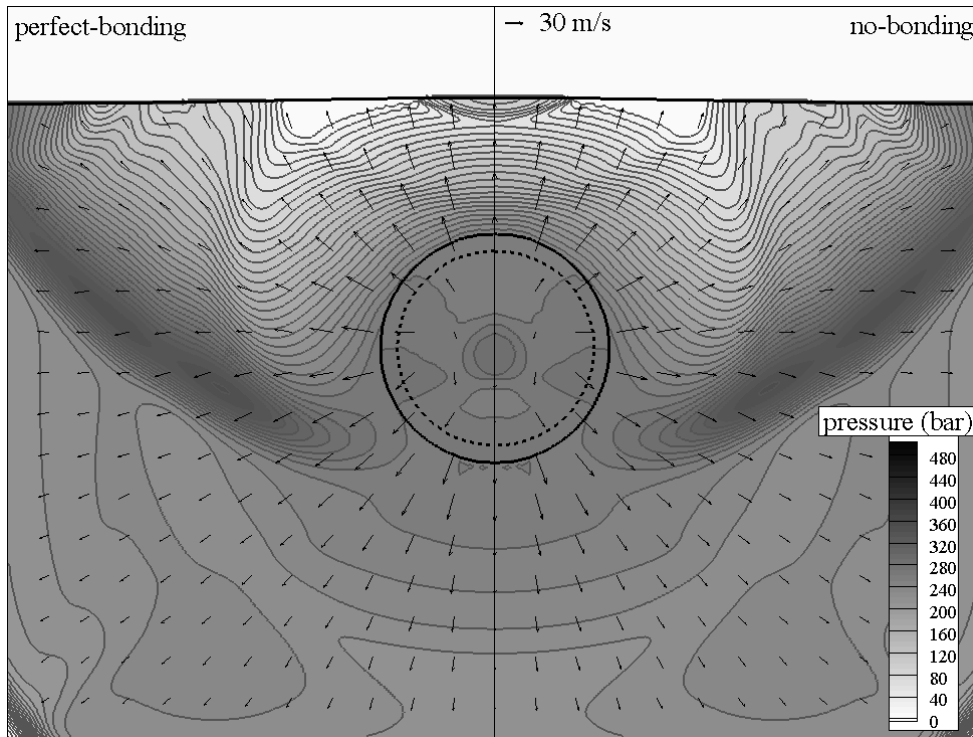


Fig. 12. Comparison of the fluid fields at $t = 0.7$ ms between the perfect- and no-bonding sandwich plates with clamped ends.

perfect- and no-bonding plates, a white cavitation region where the pressure is near zero can be found close to the front face at $t = 0.7$ ms (see Fig. 12). The collapse of the cavity leads to the second pressure peak seen immediately after $t = 0.7$ ms in Figs 4 and 5. The influence of interface bonding comes in only during the later stage, when $t > 1.0$ ms. In general, the perfect-bonding plate (on the left side of Figs 13 and 14) leads to slightly higher fluid pressure due to higher interface rigidity and thus less wave rarefaction. The perfect-bonding plate features less interface displacement and a slightly smaller expanded bubble configuration (Fig. 14).

The solid dynamics are presented in Fig. 15. The perfect- and no-bonding plates are plotted on the left and right sides, respectively. The contour levels represent the maximum principal plastic strain, which characterize the plastic yielding within the sandwich structure. Notice that the vertical dimensions have been magnified by four times. Notice that the perfect-bonding panel is acting as an integrated structure, so that the inner foam core layer exhibits bending behavior. The no-bonding plate is acting as three independent structures, where the top and bottom panels are primarily subject to bending and the middle panel (foam core) is primarily subjected to compression. By examining different time frames from the top to the bottom, one can clearly see the initiation and propagation of plastic yielding regions in the foam core layer. Plastic hinges start to form and grow near the clamped ends for the front steel plate during the later stage. Slight differences can be observed between the perfect- and no-bonding plates at the early stages ($t = 0.4$ ms). The difference becomes more significant for the later stages ($t = 0.7$ ms, $t = 1.5$ ms, and $t = 2.4$ ms). In general, the no-bonding plate features a larger plastic yielding region with higher contour levels due to the loss of interface bonding, which resulted in larger deformation of the front face and smaller deformation of the rear face. This is consistent with the nominal strain history as shown in Fig. 9. However, the no-bonding plate features a slightly larger plastic yielding region near the supports of the front face steel panels, as shown in the bottom rows of Fig. 15. Without interface bonding, the front face steel panel has to withstand more impact from the explosion, and it also transfers less energy to the back steel panel, as shown in Fig. 16.

To visualize the influence of interface bonding, the horizontal (x) and vertical (y) displacement contours are shown in Fig. 17. For the no-bonding plate, there exists significant discontinuity in the horizontal displacement contour (as shown in the top row of Fig. 17), but very little discontinuity in the vertical displacement contour (as shown in the

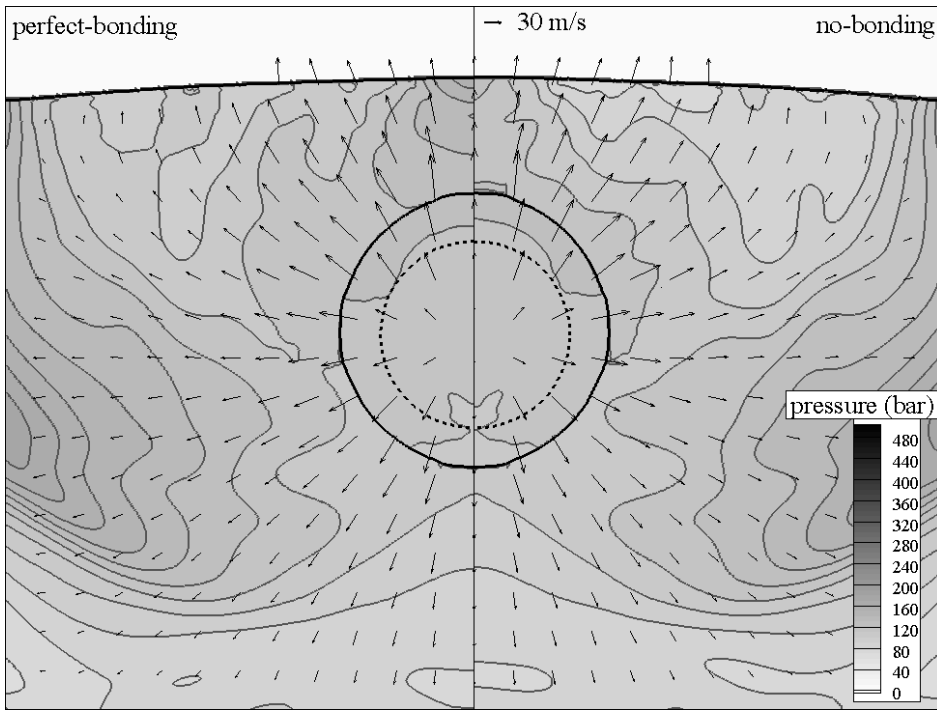


Fig. 13. Comparison of the fluid fields at $t = 1.5$ ms between the perfect- and no-bonding sandwich plates with clamped ends.

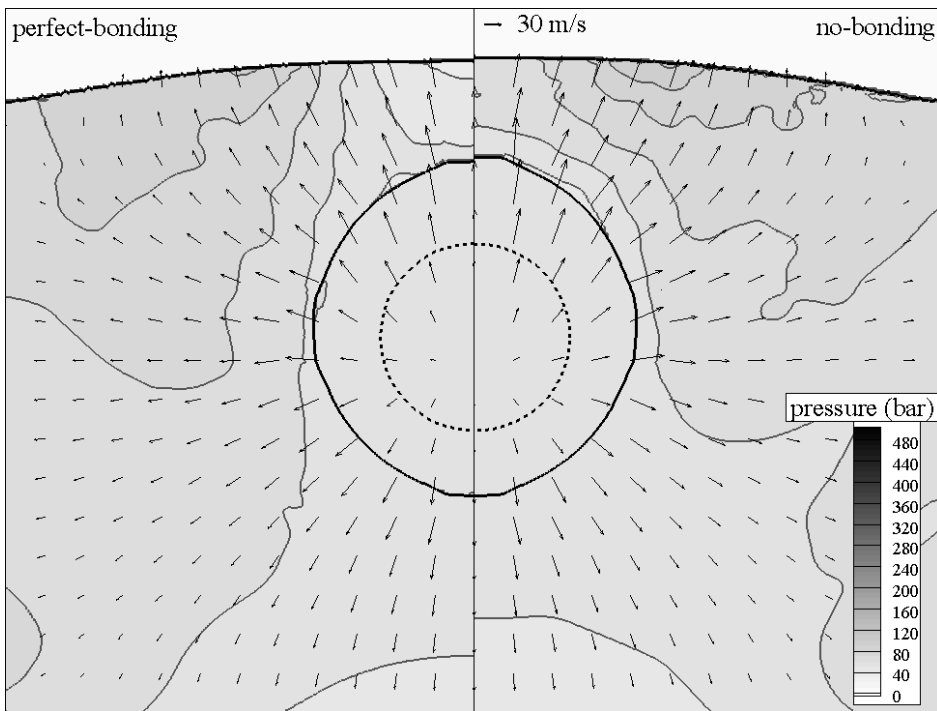


Fig. 14. Comparison of the fluid fields at $t = 2.4$ ms between the perfect- and no-bonding sandwich plates with clamped ends.

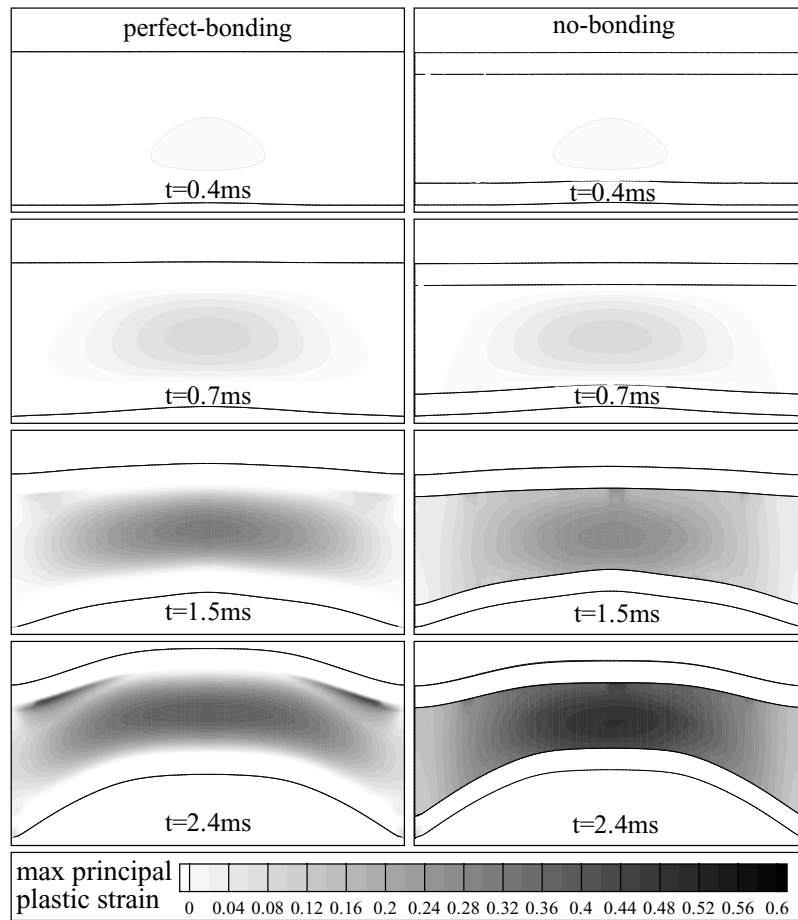


Fig. 15. Comparison of the maximum principal plastic strain contours at different time instances between the perfect- and no-bonding sandwich plates with clamped ends.

bottom row of Fig. 17). In addition, the loss of interface bonding significantly altered the horizontal displacement distributions while it had negligible influence on the vertical displacement distributions. This indicates that the loss of interface bonding causes primarily slippage between layers instead of interface delamination during the early stage of UNDEX near sandwich plates (where local buckling is not a concern).

3.5. Parametric studies

3.5.1. Face-to-core ratio

It has been shown that the no-bonding plate decreases the net energy transferred to the structure due to lower wet face pressure and higher plastic energy dissipation, which is an *advantage* from loss of interface bonding. At the same time, the no-bonding plate decreases the structural stiffness and thus leads to higher structural deformation of the front steel face, which is a *disadvantage* from loss of interface bonding. To investigate the sensitivity of system dynamics over the face-to-core thickness ratio, and to quantify the pros and cons of the loss of interface bonding, parametric studies are performed for the same core thickness of $t_c = 150$ mm and varying face thickness of $t_f = 25$ mm, $t_f = 30$ mm, and $t_f = 35$ mm. In Fig. 18, the ratio of $\psi \equiv |\chi_{NB}/\chi_{PB} - 1|$, which characterizes the influence of interface bonding, is plotted for the time interval of $t \in [1.0 \text{ ms}, 2.4 \text{ ms}]$. The generic variables χ_{NB} and χ_{PB} denote mid-span deflection of the front steel face or the net energy gained by the structure for the no-bonding and perfect bonding plates, respectively. Notice that $(\chi_{NB}/\chi_{PB} - 1)$ is positive for the mid-span deflection and

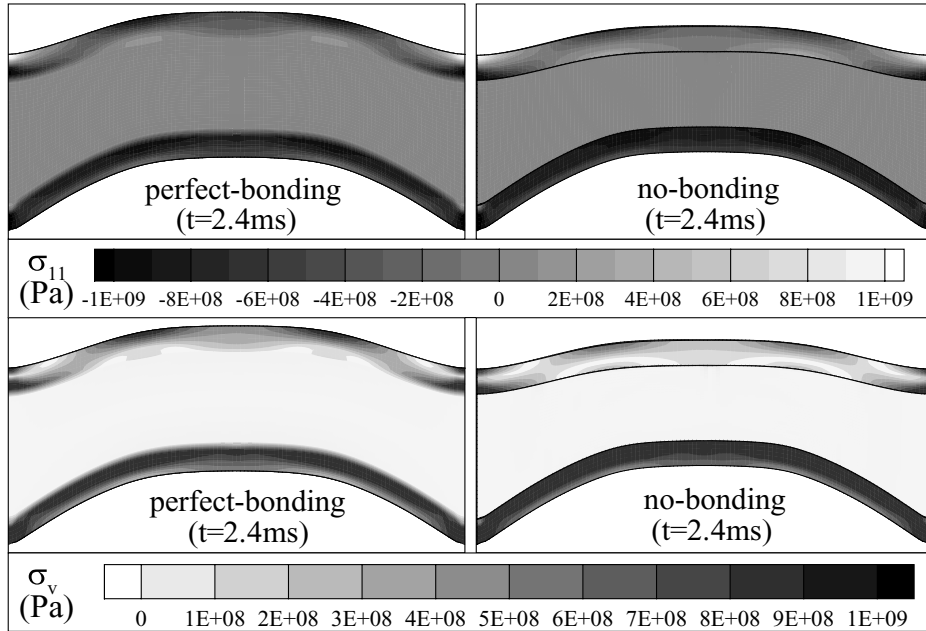


Fig. 16. Comparison of the stress distributions at $t = 2.4$ ms between the perfect- and no-bonding sandwich plates with clamped ends.

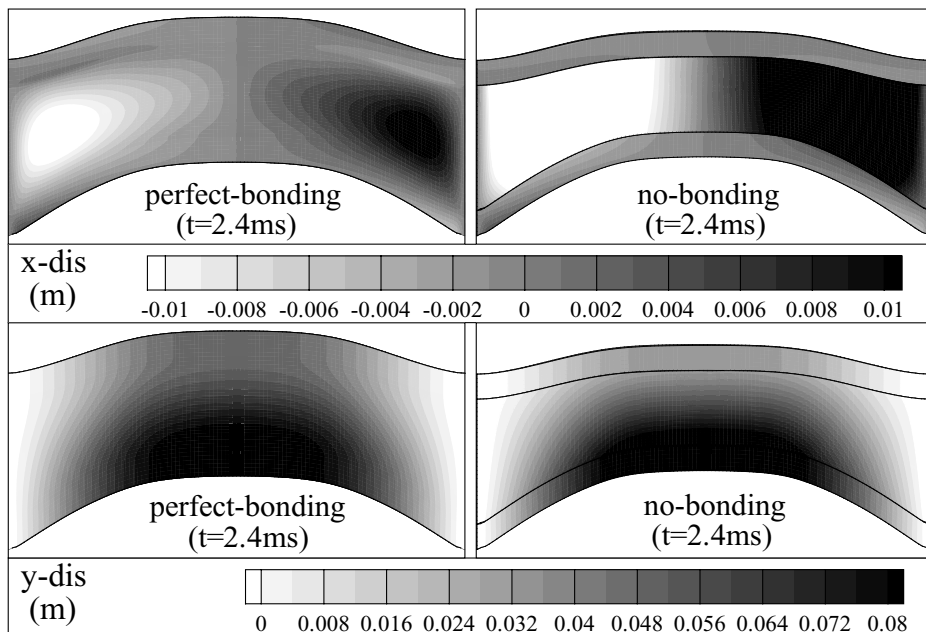


Fig. 17. Comparison of the horizontal (x-direction) and vertical (y-direction) displacement fields at $t = 2.4$ ms between the perfect- and no-bonding sandwich plates with clamped ends.

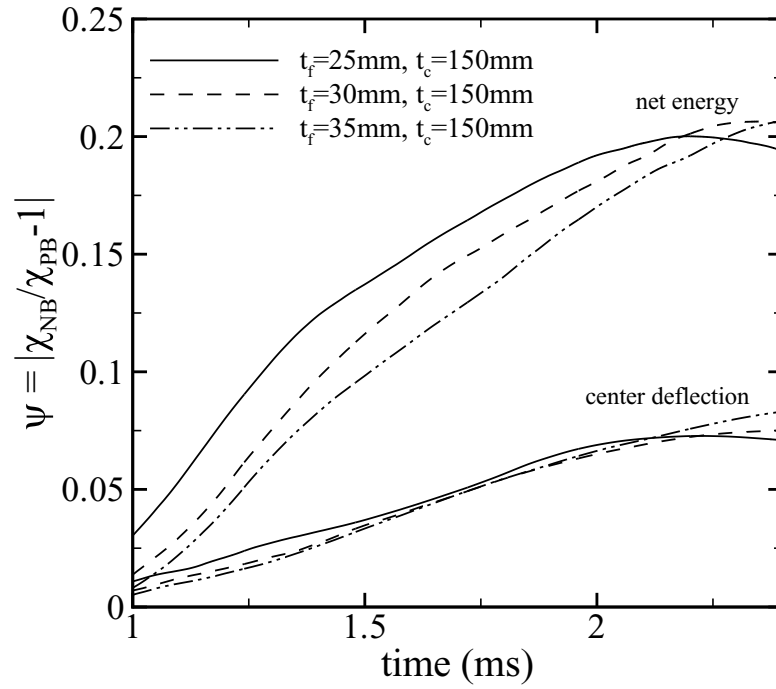


Fig. 18. Parametric studies on the influence of face-to-core thickness ratios on the mid-span deflection and net energy absorption ratios between the perfect- and no-bonding sandwich plates with clamped ends.

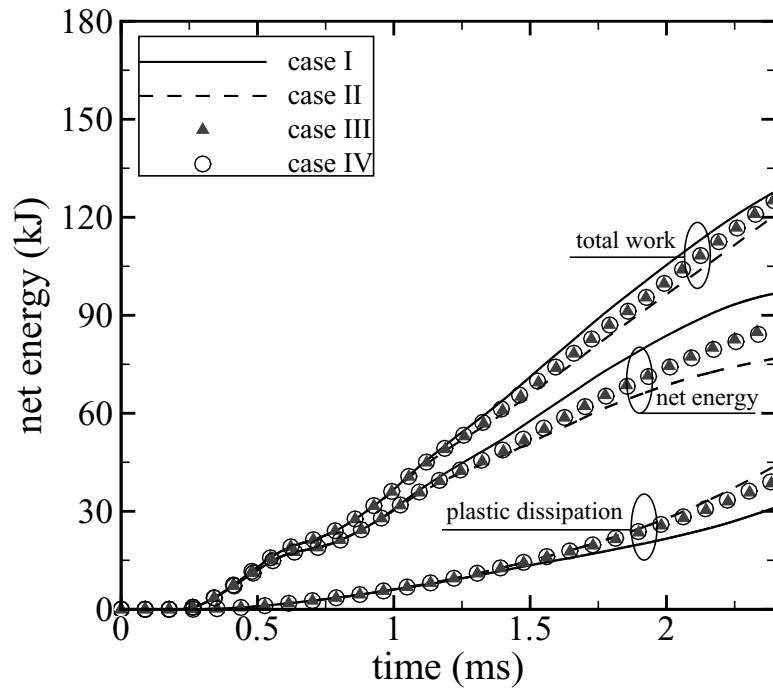


Fig. 19. Influence of the bonding sequence on the net energy transferred to the structure.

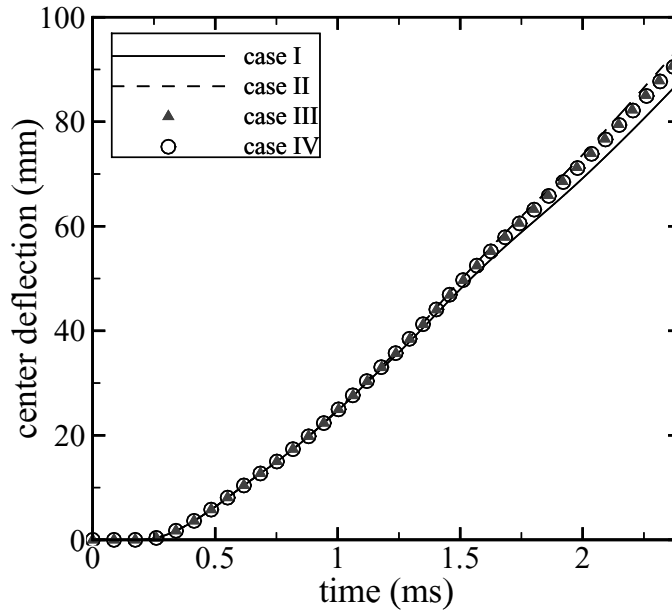


Fig. 20. Influence of the bonding sequence on the mid-span deflection.

negative for the net energy transferred. The absolute value is taken for plotting purpose. It can be seen that the *advantage* (represented by ψ for the decrease in net energy transferred) is higher than the *disadvantage* (represented by ψ for the increase in mid-span deflection). This is true for the range of face-to-core thickness ratios examined. The *advantage* increases as the face-to-core thickness ratio decreases, i.e. as the face steel plate becomes thinner relative to the foam core. This is because energy dissipation via plastic deformation of the foam core dominates for thinner face panels where most of the blast energy is transmitted and dissipated by the soft core layer. The results also show that the *advantage* (decrease in net energy transferred) is more sensitive than the *disadvantage* (increase in mid-span deflection) to varying face-to-core thickness ratios. This is because the mid-span deflection is primarily dependent on the thickness of the face panel and the influence of interfacial bonding is secondary.

3.5.2. Bonding sequence

As illustrated in Fig. 1, there are two foam-steel interfaces, namely, interface 1 and interface 2. To study the relative importance of bonding interfaces, 1 or 2, results from all four cases (as described in Section 4.2) are compared in Fig. 19. It can be seen that de-bonding at either interface 1 or 2 leads to decrease in total work done by the fluid, increase in plastic energy dissipation by the foam core, and hence decrease in net energy transferred to the structure. Cases III (de-bonding at interface 1) and IV (de-bonding at interface 2) yield almost the same energy transfer histories, and the responses are bounded by Cases I (perfect-bonding at interfaces 1 and 2) and IV (de-bonding at interfaces 1 and 2). Similarly, de-bonding at either interface 1 or 2 leads to increase in mid-span deflection due to decreased structural stiffness, as shown in Fig. 20. Cases III and IV lead to almost the identical mid-span deflection time-histories, which are also bounded by results from Cases I and IV. The study shows that the two interfaces, 1 and 2, are equally important for the energy transfer and dissipation, as well as the structural stiffness and deformation.

3.5.3. Bonding ratio

All of the previous studies assume complete bonding/de-bonding at one or two interfaces. However, due to other practical considerations, the interfaces may only be partially de-bonded. As shown in Fig. 2, there are two typical configurations, namely, de-bonding with interruptions (scheme A) and without interruptions (scheme B). Notice that the total length of de-bonding interfaces is L_{nb} for both schemes. To investigate the effectiveness of these two schemes, parametric studies are performed for varying de-bonding ratio of $\xi_{nb} \equiv L_{nb}/L$ ranging from zero to unity. Notice that L is the total length of the sandwich panel. As shown in Fig. 21, the maximum energies (the

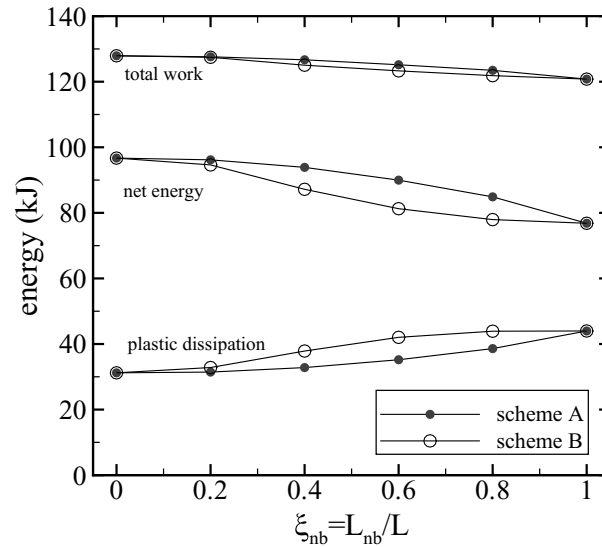


Fig. 21. Influence of the de-bonding ratios on the energy transfer histories.

value at $t = 2.4$ ms) are plotted as the function of ξ_{nb} for both schemes. It can be seen that the plastic energy dissipation monolithically increases with increasing de-bonded length, while the total work done by the fluid and the net energy gained by the structure monolithically decreases with increasing de-bonded length. The results show that the plastic energy dissipation increases more rapidly for scheme *B* than scheme *A*. Similarly, the total work and net energy decrease more rapidly for scheme *B* than for scheme *A*. This is because the de-bonding areas are continuous for scheme *B* while they are discontinuous for scheme *A*. As discussed in Section 4.4, interface slippage is the dominant mode of interface de-bonding, and it is concentrated near the quarter span, away from the center and ends. The interfacial slippage requires certain length to accumulate. Thus, the continuous interfacial de-bonding is more influential than the discontinuous configuration to facilitate the slippage and thus energy dissipation.

4. Conclusions

In the current work, the influence of interfacial bonding on the transient response of typical sandwich plates subject to underwater explosions was systematically investigated. It was found that un-bonded sandwich plates receive lower shock energy transmitted from the fluid. In addition, more energy is un-bonded sandwich plates dissipate more energy through plastic deformation of the foam core. Thus, interfacial de-bonding leads to lower net energy transferred from the explosion to the target structure. The interfacial slippage was found to be the dominant mode of the de-bonding behavior. Interfacial separation is negligible for the primary and early stages of shock-structure interaction. Despite of the more favorable energy dissipation behavior, the loss of interface bonding increases the deformation at the front steel face due to reduction in effective stiffness. However, parametric studies showed that the *advantage* (decrease in net energy transferred to the structure) is more significant than the *disadvantage* (increase in mid-span deflection at the front steel face). Thus, active/passive interfacial de-bonding mechanisms may be beneficial to achieve more blast-resistant designs. Parametric studies were also performed between the discontinuous and continuous de-bonding configurations. Results showed that it is more effective to make the de-bonding area continuous without interruptions.

Acknowledgments

The authors are grateful to the Office of Naval Research (ONR) and Dr. Ki-Han Kim (program manager) for their financial support through grant numbers N00014-07-1-0491 and N00014-08-1-0475.

References

- [1] H.N.G. Wadley, Multifunctional periodic cellular metals, *Proceedings of the Royal Society A* **364** (2006), 31–68.
- [2] H.J. Rathbun, D.D. Radford, Z.Y. Xue, M.Y. He, J. Yang, V.S. Deshpande, N.A. Fleck, J.W. Hutchinson, F.W. Zok and A.G. Evans, Performance of metallic honeycomb-core sandwich beams under shock loading, *International Journal of Solids and Structures* **43** (2006), 1746–1763.
- [3] J.W. Hutchinson and Z.Y. Xue, Metal sandwich plates optimized for pressure impulses, *International Journal of Mechanical Sciences* **47** (2005), 545–569.
- [4] N.A. Fleck and V.S. Deshpande, The resistance of clamped sandwich beams to shock loading, *Journal of Applied Mechanics* **71** (2004), 386–401.
- [5] T. Rabczuk, J.Y. Kim, E.Samaniego and T. Belytschko, Homogenization of sandwich structures, *International Journal for Numerical Methods in Engineering* **61** (2004), 1009–1027.
- [6] Z.Y. Xue and J.W. Hutchinson, Constitutive model for quasi-static deformation of metallic sandwich cores, *International Journal for Numerical Methods in Engineering* **61** (2004), 2205–2238.
- [7] V.S. Deshpande and N.A. Fleck, One-dimensional response of sandwich plates to underwater shock loading, *Journal of the Mechanics and Physics of Solids* **53** (2005), 2347–2383.
- [8] X. Qiu, V.S. Deshpande and N.A. Fleck, Impulsive loading of clamped monolithic and sandwich beams over a central patch, *Journal of the Mechanics and Physics of Solids* **53** (2005), 1015–1046.
- [9] M.T. Tilbrook, V.S. Deshpande and N.A. Fleck, The impulsive response of sandwich beams: analytical and numerical investigation of regimes of behavior, *Journal of the Mechanics and Physics of Solids* **54** (2006), 2242–2280.
- [10] V.S. Deshpande, A. Heaver and N.A. Fleck, An underwater shock simulator, *Proceedings of the Royal Society A* **462** (2006), 1021–1041.
- [11] Z.Y. Xue and J.W. Hutchinson, Crush dynamics of square honeycomb sandwich cores, *International Journal for Numerical Methods in Engineering* **65** (2006), 2221–2245.
- [12] S. Lee, F. Barthelat, J.W. Hutchinson and H.D. Espinosa, Dynamic failure of metallic pyramidal truss core materials-experiments and modeling, *International Journal of Plasticity* **22** (2006), 2118–2145.
- [13] D.D. Radford, G.J. Mcshane, V.S. Deshpande and N.A. Fleck, The response of clamped sandwich plates with metallic foam cores to simulated blast loading, *International Journal of Solids and Structures* **43** (2006), 2243–2259.
- [14] G.J. McShane, V.S. Deshpande and N.A. Fleck, The underwater blast resistance of metallic sandwich beams with prismatic lattice cores, *Journal of Applied Mechanics* **74** (2007), 352–364.
- [15] Y. Liang, A.V. Spuskanyuk, S.E. Flores, D.R. Hayhurst, J.W. Hutchinson, R.M. McMeeking and A.G. Evans, The response of metallic sandwich panels to water blast, *Journal of Applied Mechanics* **74** (2007), 81–99.
- [16] A.Vaziri and J.W. Hutchinson, Metal sandwich plates subject to intense air shocks, *International Journal of Solids and Structures* **44** (2007), 2021–2035.
- [17] L.F. Mori, S.Lee, Z.Y. Xue, A. Vaziri, D.T. Queheillalt, K.P. Dharmasena, H.N.G. Wadley, J.W. Hutchinson and H.D. Espinosa, Deformation and fracture modes of sandwich structures subject to underwater impulsive loads, *Journal of Mechanics of Materials and Structures* **2** (2007), 1981–2006.
- [18] R.M. McMeeking, A.V. Spuskanyuk, M.Y. He, V.S. Deshpande, N.A. Fleck and A.G. Evans, An analytic model for the response to water blast of unsupported metallic sandwich panels, *International Journal of Solids and Structures* **45** (2008), 478–496.
- [19] Y.L. Young, Z. Liu and W. Xie, Fluid-structure and shock-bubble interaction effects during underwater explosions near composite structures, *Journal of Applied Mechanics* **76**(5), 051303.
- [20] Z. Liu, W. Xie and Y.L. Young, Numerical modeling of complex interactions between underwater shocks and composite structures, *Computational Mechanics* **43**(2) (2008), 239–251.
- [21] W. Xie, Z. Liu and Y.L. Young, Application of a coupled Eulerian-Lagrangian method to simulate interactions between deformable composite structures and compressible multiphase flow, *International Journal for Numerical Methods in Engineering*, Published online in Wiley InterScience (www.interscience.wiley.com). DOI: 10. 1002/nme.2667.
- [22] T.G. Liu, B.C. Khoo and W.F. Xie, Isentropic one-fluid modelling of unsteady cavitating flow, *Journal of Computational Physics* **201** (2004), 80–108.
- [23] T. Liu, B.C. Khoo and K.S. Yeo, Ghost fluid method for strong shock impacting on material interface, *Journal of Computational Physics* **190** (2003), 651–681.
- [24] S. Osher and J.A. Sethian, Fronts propagating with curvature-dependent speed: Algorithms based on hamilton-jacobi formulations, *Journal of Computational Physics* **79** (1988), 12–49.
- [25] ABAQUS, ABAQUS Version 6.5 Documentation, ABAQUS, Inc., 1080 Main Street, Pawtucket, RI 02860, 2005.



Hindawi

Submit your manuscripts at
<http://www.hindawi.com>

